Multisite EPR oximetry from multiple quadrature harmonics

R. Ahmad [a,*], S. Som [b], D.H. Johnson [a], J.L. Zweier [a], P. Kuppusamy [a], L.C. Potter [c]

[a] Davis Heart and Lung Research Institute, Department of Internal Medicine, The Ohio State University, Columbus, OH 43210, USA
[b] School of Electrical and Computer Engineering, Georgia Institute of Technology, Atlanta, GA 30308, USA
[c] Department of Electrical and Computer Engineering, The Ohio State University, Columbus, OH 43210, USA

ABSTRACT

Multisite continuous wave (CW) electron paramagnetic resonance (EPR) oximetry using multiple quadrature field modulation harmonics is presented. First, a recently developed digital receiver is used to extract multiple harmonics of field modulated projection data. Second, a forward model is presented that relates the projection data to unknown parameters, including linewidth at each site. Third, a maximum likelihood estimator of unknown parameters is reported using an iterative algorithm capable of jointly processing multiple quadrature harmonics. The data modeling and processing are applicable for parametric lineshapes under nonsaturating conditions. Joint processing of multiple harmonics leads to 2–3-fold acceleration of EPR data acquisition. For demonstration in two spatial dimensions, both simulations and phantom studies on an L-band system are reported.

© 2011 Elsevier Inc. All rights reserved.

1. Introduction

Any imbalance in tissue oxygen levels may affect metabolic homeostasis and lead to pathophysiological conditions [1]. For instance, the role of hypoxia in cancer treatment [2] and wound healing [3] has been well documented. Hence, a precise knowledge of the levels of oxygen in the tissue of interest is of great importance in our ability to understand the mechanism of pathogenesis and to develop strategies to correct the imbalance.

Electron paramagnetic resonance (EPR) is a branch of spectroscopy in which electrons with unpaired spins, when placed in a magnetic field, absorb electromagnetic radiation to transition from a low energy level to a high energy level. Environment-dependent spectral changes of paramagnetic materials have led to widespread biological application of EPR, including measurement of pO_2 [4], pH [5], perfusion [6], redox [7], and detection of short-lived radicals [8].

The measurement of oxygen concentration or pO_2 by EPR involves the use of an exogenous probe consisting of paramagnetic material in either particulate (solid) or soluble form. The reversible changes in the EPR linewidth of the probe caused by the interaction [9] of two paramagnetic species – molecular oxygen and the probe – have been used to quantify pO_2. Despite the unique advantages of EPR oximetry [4], its transition to broad in vivo application has been slow. Some of the technical problems encountered in EPR

oximetry include: requirement of nontoxic exogenous probes, nonresonant absorption resulting in unwanted heating of aqueous samples and small penetration depth at higher frequencies, and poor signal-to-noise ratio (SNR) resulting in long acquisition times at lower frequencies.

For continuous wave (CW) EPR, the data are collected by measuring the absorption of electromagnetic radiation, usually in the microwave range, by paramagnetic species in the presence of an external magnetic field. For imaging applications, an additional magnetic field in the form of a linear magnetic field gradient is applied to provide spatial encoding. Recent efforts to accelerate EPR data collection include both hardware and algorithm developments. For example, overmodulation [10], fast scan [11], rapid scan [12], pulsed EPR [13], parametric modeling [14], adaptive and uniform data sampling [15], digital detection [16–18], and multisite oximetry [19,20] have shown potential to accelerate the acquisition process.

Digital detection, employing a digital heterodyne reception, simultaneously collects absorption and dispersion spectra across multiple harmonics. Digital detection offers significant advantages over the traditional homodyne phase-sensitive detection (PSD), which enables the collection of only one harmonic component. While digital detection increases the amount of EPR data collected in a given time and allows for the flexibility of retrospective signal processing, multisite EPR oximetry, under spatially sparse probe distributions, reformulates an otherwise large problem to a smaller problem with lesser unknowns. Independently, both digital detection and multisite oximetry have been shown to reduce the acquisition time for EPR oximetry. In this work, we present a framework

* Corresponding author. Address: 420 W 12th Ave., Suite 126A, Columbus, OH 43210, USA. Fax: +1 614 292 8454.
E-mail address: Rizwan.Ahmad@osumc.edu (R. Ahmad).

to take advantage of both these developments simultaneously. Multiharmonic projection data from digital detection are jointly processed to estimate linewidth information at multiple locations. Simulations and experimental data suggest that acquisition and processing of multiple harmonics further accelerates multisite oximetry by a factor of 2–3.

The remainder of the paper is organized as follows: Section 2 provides a brief overview of digital detection and multisite oximetry and describes the proposed data modeling that connects digital detection data to multisite oximetry; Section 3 presents results from both simulation and L-band multisite oximetry using a phantom; Section 4 includes discussion; Section 5 summarizes the conclusions; and Appendices A and B provide derivations of applicable data models.

2. Methodology

2.1. Receiver overview

The details of the digital receiver used to collect multiharmonic projection data have been described before [17] and only a brief synopsis is provided here. The microwave signal reflected from the resonator is amplified and bandpass filtered before it is sampled in channel 1, C_1, of the analog-to-digital converter (ADC). By sampling at a rate, ω_s, below the carrier frequency, ω_c, aliases of the bandpass signal are replicated periodically. An appropriate selection of ω_s ensures that the replicas of the signal are disjoint in frequency, and hence that aliasing artifacts are avoided. For example, with $\omega_c = 2\pi \times 1.28 \times 10^9$ rad/s and $\omega_s = 2\pi \times 400 \times 10^6$ rad/s, an alias of the original bandpass microwave signal is centered at $2\pi \times 80 \times 10^6$ rad/s (i.e., $\omega_c - k\omega_s$ for $k = 3$). Thus, sampling effectively provides demodulation to a digital intermediate frequency (IF) signal.

The microwave source signal is likewise bandpass filtered and is sampled in channel 2 of the ADC, thereby providing a reference for digital demodulation from IF to baseband. Specifically, the contents of C_1 are digitally multiplied with the contents of C_2 and its Hilbert transform to generate in-phase (Y_I) and out-of-phase (Y_Q) baseband channels, respectively. While the two channels of the ADC are time-locked by virtue of a common sampling clock, the sampling clock is not time-locked to the microwave source in this architecture. Both Y_I and Y_Q are then digitally cross-correlated with sinusoidal waveforms at the modulation frequency ω_m and its multiples to extract quadrature harmonics $y_{I,1}, y_{I,2}, y_{I,3} \ldots$, and $y_{Q,1}, y_{Q,2}, y_{Q,3} \ldots$, respectively. The sampled data streams from C_1 and C_2 are decomposed into small blocks, and all the postprocessing is carried out on a block-by-block basis. We use the notations C_1 and C_2 to describe the physical channels of the dual-channel ADC, while the notations I and Q are reserved for the channels that describe quadrature baseband data or extracted EPR quadrature harmonics.

Although the ADC was capable of sampling at a rate up to 500 MHz, we used a lower sampling frequency of 100 MHz. A disadvantage of low sampling rate is the decrease in effective vertical resolution of the ADC [21]. A limited (8 GB) on-board ADC memory was not adequate for higher sampling rates for the long scans required at high magnetic gradient projections. Traditional automatic frequency control (AFC) circuitry [22], employing a PSD, was used to lock the ω_c to the resonance frequency of the resonator. The time-constant of the AFC was kept large enough to ensure that there was no AFC response to ω_m or any of its multiples. A Bruker field controller (ER 032M) was used to sweep the magnetic field.

2.2. Multisite oximetry overview

Multisite oximetry is an EPR-based method that allows measuring oxygen from multiple sites simultaneously, without performing the time consuming spectral-spatial imaging. In 1993, Smirnov et al. [23] proposed an EPR-based multisite oximetry method. Later, Grinberg et al. [19] suggested a similar but improved method. By collecting two projections along a single magnetic gradient orientation, each projection with a different gradient strength, the pO$_2$ values at multiple sites are estimated using a convolution-based fitting method. This approach has been applied to study cerebral ischemia in rats [24]. The method relies on identifying and collecting projections for which signals from various sites minimally overlap and can be visually separated. Also, its application is strictly limited to the Lorentzian lineshape.

Subsequently, Som et al. [20] suggested a more comprehensive framework for multisite oximetry. The key assumptions made are: (i) the EPR spectrum belongs to a known parametric function family; (ii) the probe distribution is spatially sparse, i.e., the localized spin pockets, called sites, constitute only a small fraction of the field-of-view (FOV); and (iii) each site exhibits a single pO$_2$ value. Under these assumptions, each spatial voxel is characterized by an unknown spin density and linewidth, and the proposed forward model relates the collected projection data to these unknowns. These parameters are then estimated jointly from a small set of projections. This method not only provides an estimate of linewidth (pO$_2$) at each site but also reconstructs the spatial distribution of the sites. This approach does not impose any restrictions on the geometry or number of sites. It also does not require a priori knowledge of site locations or a suitable gradient orientation for a given geometry of sites. This approach is a supplement and not a direct alternative to the previous multisite methods which are more restrictive but, when applicable, can offer larger acquisition time savings.

The method proposed in this paper is an extension of our previous work [20]. Unlike the previous version, which solves the multisite problem using undermodulated first harmonic absorption data, this method is capable of jointly processing overmodulated projection data across multiple harmonics for accelerated multisite oximetry.

2.3. Forward modeling

Although it is possible to extend the previous forward model [20] from undermodulated first harmonic absorption data to overmodulated multiharmonic data, here we have adopted a different strategy to avoid the lengthy derivations and extensive computational burden associated with the previous model, which requires computing integrals of the lineshape over the 4D spectral-spatial domain. In the case of overmodulation, the mathematical expressions that describe lineshape become increasingly complex as we move to higher harmonics, making the derivation of analytical expressions extremely tedious and the related coding prone to errors.

Consider a spectral-spatial object with one spectral and three spatial dimensions. The object contains $U \geqslant 2$ spatially nonoverlapping EPR active sites, each occupying a small fraction of the spatial FOV. The voxels that do not belong to any of the sites have zero intensity. Each site may possess a different lineshape and microwave phase α which are assumed to be uniform across the spatial extent of a single site. The parametric expression of the lineshape is known but the actual lineshape parameters, such as linewidth, are unknown.

We can decompose the object into U unique spectral-spatial subobjects, each with the same FOV as the original object but containing only one EPR active site. An EPR projection of a subobject is equivalent to the spatial profile of the subobject convolved with the lineshape of the site in that subobject. The spatial profile for a particular gradient orientation is computed by the Radon transform of the spatial component of the subobject. Both the spatial

profile and the lineshape are horizontally compressed and vertically scaled before convolution, and the amount of compressing and scaling is dictated by the magnetic gradient magnitude. The projection of the original object is simply a summation of the projections from all subobjects.

To generate different harmonic components of a given projection, the spatial profile is convolved with different harmonic components of the overmodulated spectrum described by Robinson et al. [25]. The forward modeling concept is illustrated in Fig. 1 for a 2D spatial and 1D spectral object. For brevity, only the first harmonic absorption component is displayed. See Appendix A for the derivation of the forward model.

The application of the forward model described above requires the knowledge of site locations which are generally not known in advance except for special cases, such as NMR-EPR coimaging [26], where high-resolution MRI can provide the location of EPR sites. Here, we adopt a two-stage approach with coherent and incoherent variations at stage 1. For the case of homogeneous microwave phase, a coherent stage 1 reconstruction uses ℓ_1 regularized minimization of an approximate linear model to obtain a low-resolution distorted spin density distribution. To linearize the problem, all unknowns other than spin density are assigned approximate user-defined values. The extent of distortion depends on the disagreement between the true values of the unknowns and their user-defined approximate values adopted in the linearized model.

We have observed from simulated data that if the user-defined value of the microwave phase is not close to the true value then the
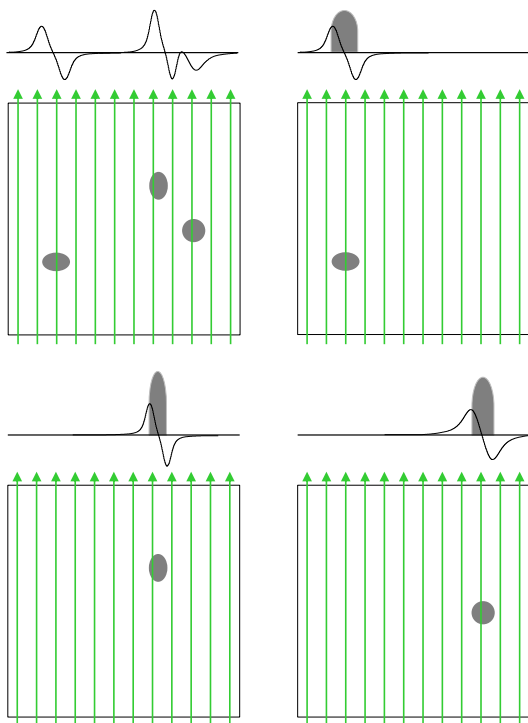
distortion in the resulting stage 1 reconstruction is significant. For applications where microwave phase not only drifts over time but also changes from site to site [27], a single-user defined value of microwave phase may result in distortion in the stage 1 reconstruction. Therefore, for this case we propose a nonlinear incoherent reconstruction scheme for stage 1 as outlined in Appendix B. The idea is to first make the unknown spin density distribution complex-valued and thus accommodate the spatial variations in the phase. The second step of the incoherent reconstruction is to curve-fit the root-sum-square (RSS) of the quadrature harmonics instead of fitting the quadrature components explicitly. This step removes the phase variations from projection to projection. The downside of the incoherent approach for stage 1 is a doubling of problem size and a nonlinear curve-fitting (Eq. (B.6)).

2.4. Linewidth estimation

An approximate spin density map generated from stage 1, by either coherent or incoherent reconstruction, is first segmented into U segments. Circles (in 2D spatial case) or spheres (in 3D spatial case) centered at the centroids of the segments are used to approximate each site in space. The size of the circles (spheres) is selected to accommodate uncertainties associated with the model approximations for stage 1.

For stage 2, all unknown parameters are assumed to be constant from projection to projection except microwave phase difference at the input channels of the ADC, which, for our implementation of the digital receiver, may gradually change over time due to frequency drifts [17]. The unknown forward model parameters that are jointly estimated in stage 2 include: linewidths (one per site); modulation amplitudes (one per site); spin densities (for all voxels at each site); center field (one per projection); microwave phase (one per site); microwave phase difference between the two ADC channels (one per projection); and dc baseline shift (one for each harmonic component per projection). We used nonlinear least-squares curve-fitting to estimate the unknown parameters jointly. For stage 2, no regularization term was used because the problem was well-conditioned.

3. Results

In this section, we validate the proposed data modeling using both computer simulations and L-band multisite oximetry data. To reduce the data processing time, we restricted both the simulation studies and lab experiments to two spatial dimensions. These studies also draw comparisons among undermodulated first harmonic from the *I* channel, overmodulated first harmonic from the *I* channel, and three pairs of quadrature harmonics with overmodulation.

3.1. Simulation

We performed the simulations on a 2D digital phantom with the spatial size of 40×40 pixels. The phantom carried five sites each with 2×2 pixels, and all other pixels had zero intensity. All pixels belonging to one site were assigned the same intensity value. The intensity values across different sites varied from 0.7 to 1.0.

Each site of the phantom was assigned a modulation-distorted Lorentzian lineshape defined in terms of linewidth, modulation amplitude, and microwave phase. The linewidth values used for the five sites were 0.32 G, 0.36 G, 0.40 G, 0.44 G, and 0.48 G. To mimic experimental conditions, the modulation amplitude was varied randomly, from site to site, within ±10% of the nominal value. The microwave phase was also allowed to vary randomly from site to site. A gradual microwave phase drift, from projection to projection,

Fig. 1. Illustration of the forward modeling concept. The top-left square panel displays the spatial dimensions of a 2D spatial, 1D spectral object with three EPR active sites ($U = 3$). The other three square panels show the decomposition of the object into three subobjects. The vertical arrows indicate the lines of integration for the Radon transform for a particular gradient orientation. The shaded areas residing on the horizontal lines are the spatial profiles resulting from the Radon transform of the 2D spatial subobjects. These spatial profiles are then convolved with the respective lineshapes (not shown) of the subobjects to generate projections, indicated by black sold line on the horizontal axis. The final projection, shown above the top-left square panel, of the object is the sum of the projections from all the subobjects.

was simulated by adding a single random walk with a step size of 5° to the microwave phases of all sites. The value of pSNR, defined by the ratio of peak-to-peak signal and the standard deviation of noise, for the zero-gradient projection was selected to be 30. A scan time (which affects the SNR) for each projection was proportional to $\lceil|\tan\theta|\rceil$, with $\lceil\cdot\rceil$ denoting the next higher integer and θ denoting the spectral angle. This variable sweep time allows partial suppression of the degradation of SNR for high gradient projections. Projection angles were uniformly distributed [15] between 0 and the maximum permissible spectral angle θ_{max}. A random dc baseline was added to each harmonic component of each projection and the dc amplitude was limited to ±5% of the peak value of that component. A slow frequency drift was simulated by adding a random walk with a step size of 20 mG to the resonance location of the lineshape for each projection. Other simulation parameters were: spatial FOV diameter ΔL = 1.6 cm; spectral window ΔB = 4.8 G; maximum gradient = 12 G/cm; nominal field modulation amplitude for undermodulation = 0.12 G; nominal field modulation for overmodulation = 1.2 G; number of projections in each dataset = 16; samples per projection = 128.

A total of 24 trial runs were considered, 12 with undermodulation and 12 with overmodulation. Each trial had different site locations, noise realization, projection angle distribution, and microwave phase realization. There was no constraint on the distribution of site locations except that no two sites were allowed to touch or overlap. Therefore, we enforced a minimum distance of two pixels between the neighboring sites.

The incoherent reconstruction was used in stage 1 to approximate site locations. To solve for Eq. (B.6), we assigned the values of 0.3 G to Γ, 1.1 G to modulation amplitude (B_m), 0 to dc baseline across all projections and its harmonics, and 0 G for resonance peak drift for all projections. Fig. 2 shows fitting results for stage 1 and stage 2 for one the 16 projections for an overmodulated dataset. The structure in the residual for stage 1 is due to the mismatch between the true parameter values and user-defined approximate values. A reconstruction from the joint processing of six harmonic components is shown in Fig. 3.

Fig. 4 compares linewidth estimation from undermodulated $y_{I,1}$ (UM-1), overmodulated $y_{I,1}$ (OM-1), and joint processing of overmodulated $y_{I,1}$, $y_{Q,1}$, $y_{I,2}$, $y_{Q,2}$, $y_{I,3}$, and $y_{Q,3}$ (OM-6). For UM-1 and OM-1, since there is only one harmonic component available, the incoherent reconstruction was not possible which requires quadrature signal. Therefore, for UM-1 and OM-1 no spatial and temporal phase variations were introduced and stage 1 reconstructions was performed using previously proposed coherent reconstruction, with microwave phase set at 0°.

3.2. L-band multisite oximetry

A multisite oximetry was performed on a four-site phantom constructed with LiNc–BuO [28], a commonly used oxygen sensitive probe. The phantom consisted of four capillary tubes, each carrying 50–80 µg of LiNc–BuO. The pO$_2$ was varied in the capillary tubes by adding small quantities of sodium hydrosulfite [20] and flame sealing the tubes. The true linewidth values, measured individually under high SNR conditions, were 0.375 G, 0.367 G, 0.497 G, and 0.469 G. The data were collected on an L-band system equipped with the recently developed digital receiver [17]. We used a volume reentrant resonator with 12 mm diameter.

The experiment was repeated 12 times, 6 times with undermodulation and 6 times with overmodulation. The user defined experimental parameters were: spatial FOV diameter ΔL = 1.6 cm; spectral window ΔB = 4.8 G; maximum gradient = 12 G/cm; nominal field modulation amplitude for undermodulation = 0.12 G; nominal field modulation for overmodulation = 1.2 G; excitation power = 100 µW; number of projections = 16; and samples per
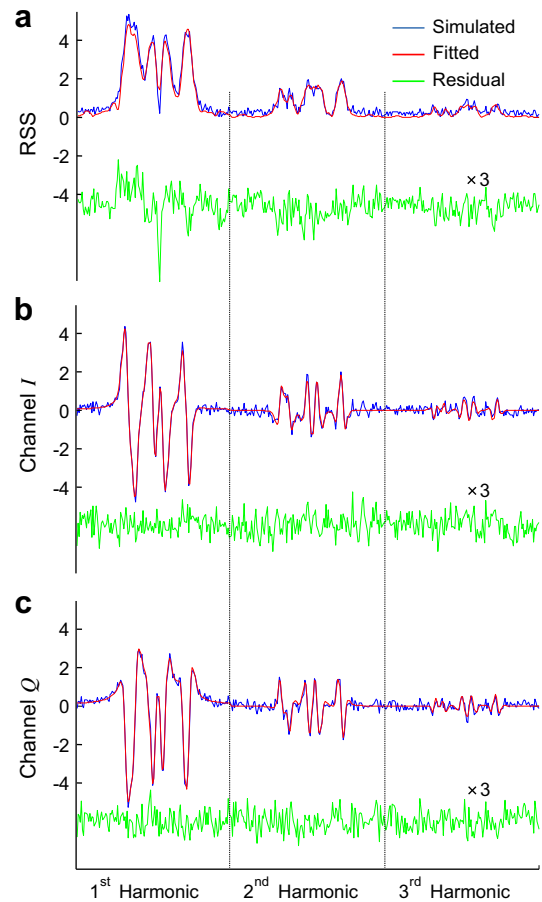

Fig. 2. Fitting results for stage 1 and stage 2 for the 2D simulated phantom shown in Fig. 3. For incoherent reconstruction of stage 1 (a), curve fitting is performed on the root-sum-square (RSS) of the simulated quadrature harmonics. For stage 2, the six quadrature harmonics (b and c) are jointly fitted. Only the maximum field gradient projection is shown, and only the first three harmonics are depicted. The two vertical dotted lines separate the three harmonics.
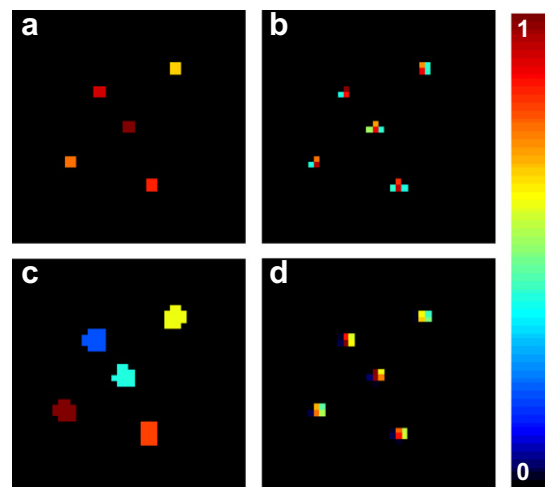

Fig. 3. Multisite reconstruction for 40 × 40 simulated phantom with five sites. Input phantom (a), stage 1 spin density reconstruction (b), image segmentation based on stage 1 (c), and the final spin density reconstruction from stage 2 (d). The reconstructions represent a spatial dimension of 11.3 × 11.3 mm^2 and image resolution of 40 × 40 pixels.

projection = 512. Each dataset varied in measurement noise and projection angle distribution. Fig. 5 shows the curve fitting for
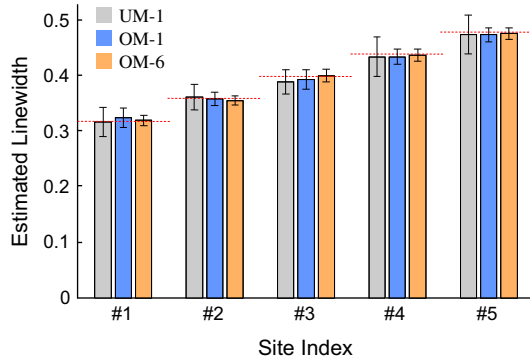
Fig. 4. Estimated linewidths for the five-site simulated phantom. Error bars represents ±2 std. UM-1 represents linewidth estimation from undermodulated $y_{I,1}$ harmonic component; OM-1 represents linewidth estimation from overmodulation $y_{I,1}$; and OM-6 represents linewidth estimation based on the joint processing of $y_{I,1}$, $y_{Q,1}$, $y_{I,2}$, $y_{Q,2}$, $y_{I,3}$, and $y_{Q,3}$. The horizontal dashed lines indicate the true linewidth values.

stages 1 and 2 for one the projections from an overmodulated data-set. A reconstruction from the joint processing of six harmonic components is shown in Fig. 6.

Fig. 7 compares linewidth estimation from undermodulated $y_{I,1}$ (UM-1), overmodulated $y_{I,1}$ (OM-1), and joint processing of overmodulated $y_{I,1}$, $y_{Q,1}$, $y_{I,2}$, $y_{Q,2}$, $y_{I,3}$, and $y_{Q,3}$ (OM-6). Due to the non-lossy nature of the sample and short acquisition time, we did not
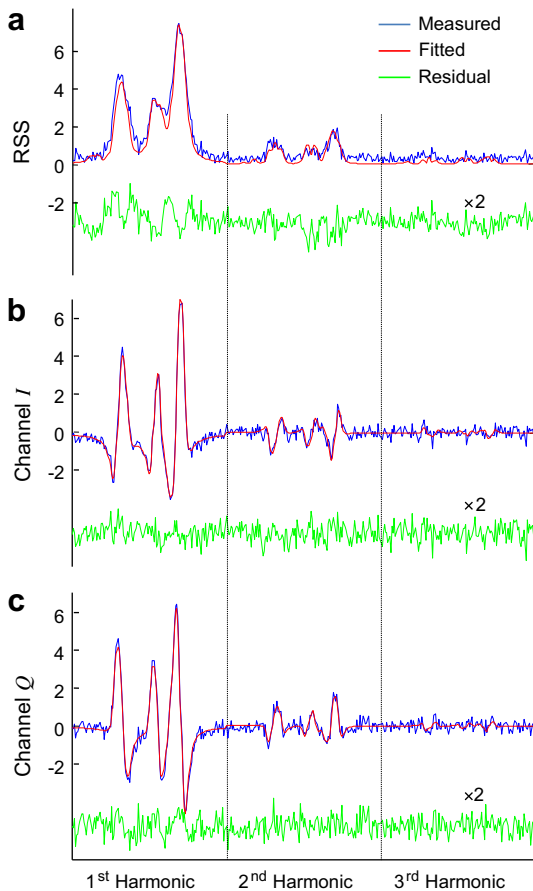
observe significant spatial or temporal changes in the microwave phase. The stage 2 estimation of unknown parameters revealed that the microwave phase stayed in the range 144° ± 4° for the entirety of the data collection across all sites. For UM-1 and OM-1, the stage 1 reconstructions was performed using the previously proposed coherent reconstruction with microwave phase fixed at 144°. For OM-6, on the other hand, the incoherent reconstruction was used for stage 1.

For the L-band experiment, a total data acquisition time for each 16-projection dataset was 150 to 180 s. Each projection had 512 samples but was downsampled to 128 samples to facilitate faster processing. Therefore, we only used approximately 40 s worth of data to estimate linewidths. Under the assumption that the sampling rate of 128 samples/projection meets the Nyquist rate, any sampling rate above 128 samples/projection does not add new information but only improves the SNR due to the added redundancy. Therefore, after-the-fact downsampling from 512 to 128 samples/projection effectively lowered the SNR by a factor of two.

4. Discussion

Multisite EPR oximetry accelerates the data acquisition by exploiting the parametric nature of the spectrum and sparseness in the spatial distribution of the probe. Digital detection, on the other hand, can accelerate the EPR oximetry data acquisition by collecting multiple quadrature field modulation harmonics. In this paper, these two developments have been brought together to achieve larger accelerations than possible by the individual developments.

We have extended our forward model, which previously was applicable only for undermodulated absorption spectra, to multiple harmonics of overmodulated spectra. Here, we have adopted a slightly different implementation of the forward model used in stage 2 to avoid lengthy analytical expressions. For stage 1, we have proposed an incoherent reconstruction scheme which can combat temporal and spatial variations in the microwave phase. The spatial variations in the microwave phase are generally present in lossy samples [27] while temporal variations may arise in the presence of microwave frequency drift. Note, a time-locked version of digital receiver [29] is not prone to temporal phase variations.

To reduce the computation time, we limited ourself to 2D oximetry because data processing for 3D case would require considerably longer processing times. Our Matlab implementation took 3–5 min for stage 1 (incoherent reconstruction) and 20 to 25

Fig. 5. Fitting results for stage 1 and stage 2 for the 2D L-band oximetry experiment. For incoherent reconstruction of stage 1 (a), curve fitting is performed on the root-sum-square (RSS) of the measured quadrature harmonics. For stage 2, the six quadrature harmonics (b and c) are jointly fitted. Only the maximum field gradient projection is shown, and only the first three harmonics are depicted. The two vertical dotted lines separate the three harmonics.
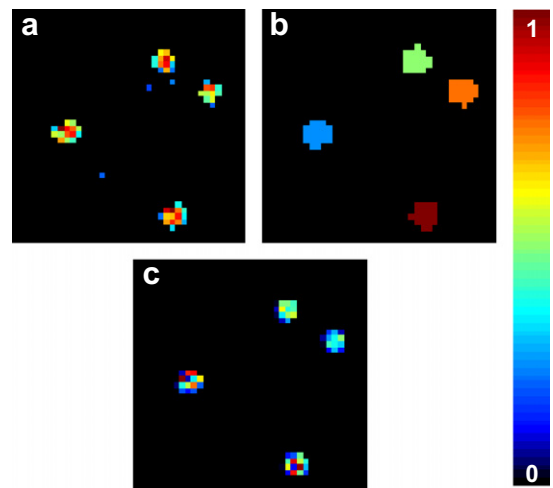

Fig. 6. Reconstruction for the four-site L-band multisite oximetry phantom. Stage 1 spin density reconstruction (a), image segmentation based on stage 1 (b), and the final spin density reconstruction from stage 2 (c). Spatial dimensions for the reconstruction are 11.3 × 11.3 mm² and image resolution is 40 × 40 pixels.
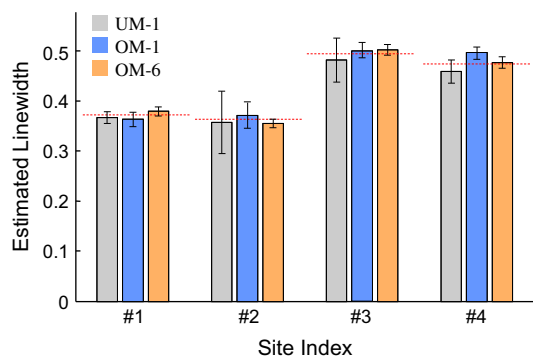
Fig. 7. Estimated linewidths for the four-site L-band multisite phantom. Error bars represents ±2 std. UM-1 represents linewidth estimation from undermodulated $y_{I,1}$ harmonic component; OM-1 represents linewidth estimation from overmodulation $y_{I,1}$; and OM-6 represents linewidth estimation based on the joint processing of $y_{I,1}$, $y_{Q,1}$, $y_{I,2}$, $y_{Q,2}$, $y_{I,3}$, and $y_{Q,3}$. The horizontal dashed lines indicate the true linewidth values.

minutes for stage 2 processing for the 2D L-band oximetry data. The total number of unknowns, which were jointly estimated in stage 2, for L-band experiments was 188. By moving to 3D oximetry, we expect that number to nearly double. Also, like the conventional EPR imaging, the proposed method can benefit from fast scanning [11]. The only technical challenge of merging the proposed method with the fast scanning is the computation burden that increases linearly with the number of projections. By employing faster computing resources, it would be possible to perform 3D oximetry from a large number of projections without downsampling.

In our implementation, we have assumed the noise power is equal in both I and Q channels. However, it has been demonstrated previously that the phase noise originating from the microwave source may impact the absorption and dispersion components of the spectrum differently, with the dispersion component generally impacted more heavily by the phase noise. Since we are estimating the microwave phase jointly, it is possible to use that estimated phase value to rotate the raw data from either C_1 or C_2 to decouple the absorption and dispersion components and use weighed least-squares to fit the resulting data [17]. This decoupling approach, however, is only accurate when there are no significant spatial phase variations.

It has been demonstrated that modulation induced lineshape broadening across different quadrature harmonics can be formulated as linear filtering of undermodulated first harmonic absorption data [30], with the filters characterized by the value of B_m. Thus it is possible, under the assumptions of a known and constant B_m and wide sweepwidth, to first convert the overmodulated multiharmonic data to undermodulated first harmonic absorption data by a deconvolution procedure [31] and then estimate the unknown parameters from the resulting data. This option is faster in terms of computation speed but more restrictive in its applicability. First, this approach assumes the value of B_m is spatially invariant and accurately known, which was not a realistic assumption for us because the modulation coils (diameter = 32 mm and separation = 15 mm) used for the L-band studies generated significant variations in B_m across the FOV. For the nominal B_m value of 1.2 G, the true B_m values as estimated in stage 2 ranged from 0.99 to 1.32 G across the four sites. Second, this approach assumes the projection data are not truncated, requiring a sweepwidth which is significantly larger than the largest linewidth as well as the largest modulation amplitude. To save acquisition time, we have opted for narrow sweepwidths for both the simulation and the experimental data. Therefore, in our case the projection data, especially at low field gradients, is severely truncated. Last, we have adopted a more direct approach in which unknown

parameters are estimated directly from the measured data instead of first reconstructing the undermodulated first harmonic absorption data by deconvolution and then estimating the unknown parameters from the resulting deconvolved data.

As observed from the experimental data, the value of B_m was not spatially uniform due to the small size of the modulation coils. In this case, a prior knowledge of B_m distribution alone may not be useful as there might not be a straight forward method to know the distribution of the probe, which is generally unknown, with respect to the B_m distribution. However, when B_m is uniformly distributed in space, an accurate calibration of B_m can be advantageous as it eliminates the necessity to estimate B_m altogether.

To separately evaluate the effects of overmodulation and multiple harmonics, we computed the root mean squared error (RMSE) for both the simulated and L-band data. The RMSE was defined as the root mean squared value of the difference between the true linewidth and the estimated linewidth across all sites and all trial runs. For the simulation data, we observed the RSME for UM-1, OM-1, and OM-6 to be 14.8×10^{-3}, 8.4×10^{-3}, 5.5×10^{-3}, respectively. For the L-band data, we observed the RSME for UM-1, OM-1, and OM-6 to be 21.6×10^{-3}, 16.6×10^{-3}, 9.8×10^{-3}, respectively.

As expected, we see an improvement in the RMSE from UM-1 to OM-1 and from OM-1 to OM-6, validating the use of overmodulation as well as multiple harmonics for multisite oximetry. The improvement, however, was less that what has been achieved for EPR spectroscopy. A smaller jump from UM-1 to OM-1 is partially due the modulation-induced line broadening, which makes the inversion more ill-posed. Also, a smaller gain from OM-1 to OM-6 is due to the high-pass nature of the higher harmonics, which diminish more rapidly with an increase in magnetic field gradient. This effect is also evident from Figs. 2 and 5 where the third harmonic has minimum energy at the maximum field gradient. Increasing the value of B_m can increase the relative strength of higher harmonics but only at the expense of lineshape broadening. Also, increasing B_m beyond a certain limit reduces the energy (sum-of-squares) in the lower harmonics. Further investigations are required to determine optimal values of B_m and maximum gradient.

5. Conclusions

In this work, we have demonstrated that multisite EPR oximetry can benefit from digital detection which is capable of generating multiple field modulation harmonics in quadrature. A forward model is presented that relates the measured projection data across multiple harmonics to the unknown parameters including linewidths at multiple sites. A joint processing of multiple harmonics reduces the RMSE error in the estimation of linewidth by a factor of 1.5–1.7, which translates to approximately 2–3-fold reduction in the acquisition time. The acceleration is in addition to what can be provided by overmodulating a single harmonic component. The simulation studies and experimental data are presented for 2D oximetry but can be readily extended to 3D oximetry.

Acknowledgments

Appendix A. Forward model for stage 2

Here, we describe a forward model that relates the unknowns belonging to a spectral-spatial object as well as the EPR measurement process to the measured CW EPR projection data. We make the following assumptions about the object and the measurement

process: (i) the spectral-spatial object is bounded in both spectral and spatial domains; (ii) EPR lineshape is complex and belongs to a parametric family of functions; (iii) EPR probe is spatially distributed to form U nonoverlapping sites; (iv) each site, consisting of one or more voxels, has a uniform but unknown modulation amplitude, linewidth, and microwave phase; (v) there is no signal distortion due to RF power saturation; and (vi) the main magnetic field is swept in discrete steps for each projection.

If the spatial location of the probe sites is known, we can decompose the multisite spectral-spatial object into U subobjects, each containing only one site. Let f_u be one of the subobjects with one spectral and one or more spatial dimensions, defined by

$$f_u(\vec{r}, B) = \mathcal{E}_u(\vec{r})\,\mathcal{L}_u(B; \vec{r})\, e^{j\alpha_u(\vec{r})}, \tag{A.1}$$

where $\vec{r}$ represents the spatial coordinates of the object, $\mathcal{E}_u(\vec{r})$ represents a positive real-valued distribution of the probe spin density; $\mathcal{L}_u(B; \vec{r})$ denotes the EPR lineshape, at $\vec{r}$, as a function of magnetic field B; j is the imaginary unit; and $\alpha_u(\vec{r})$ represents a spatially varying microwave phase for the subobject u.

The function $\mathcal{L}_u(B; \vec{r})$ is complex valued, with real part, $\mathcal{L}_u^a(B; \vec{r})$, pertaining to the absorption component and the imaginary part, $\mathcal{L}_u^d(B; \vec{r})$, pertaining to the dispersion component of the EPR signal. In the case of Lorentzian lineshape, both the components can be expressed as

$$\mathcal{L}_u^a(B; \vec{r}) = \mathrm{Re}(\mathcal{L}_u(B; \vec{r})) = \frac{\Gamma_u(\vec{r})}{(B - B_c)^2 + \Gamma_u^2(\vec{r})},$$

$$\mathcal{L}_u^d(B; \vec{r}) = \mathrm{Im}(\mathcal{L}_u(B; \vec{r})) = \frac{B - B_c}{(B - B_c)^2 + \Gamma_u^2(\vec{r})}, \tag{A.2}$$

where $\Gamma_u(\vec{r})$ is the half width at half-maximum linewidth at location $\vec{r}$; B_c is the location of the resonance peak; and $\mathrm{Re}(\cdot)$ and $\mathrm{Im}(\cdot)$ represent real and imaginary parts, respectively.

For each subobject, we assume the site encompasses a small region, i.e., $\mathcal{E}_u(\vec{r})$ is nonzero only for a small localized region. Therefore, we assume there is no lineshape or microwave phase variations across the spatial extent of a single site. Under this spatial invariance of lineshape and microwave phase, we can write $\Gamma_u(\vec{r}) = \Gamma_u$, $\mathcal{L}_u(B; \vec{r}) = \mathcal{L}_u(B)$, and $\alpha_u(\vec{r}) = \alpha_u$.

Let $B_{\mathrm{ext}}(\vec{r})$ be the net external magnetic field given by

$$B_{\mathrm{ext}}(\vec{r}) = B_0 + b + B_{\mathrm{m}}\cos(\omega_{\mathrm{m}} t) + \vec{G} \cdot \vec{r}, \tag{A.3}$$

where B_0 is the static magnetic field with magnitude set close to the resonance field B_c; b is a variable offset from B_0 used to sweep the field over the range of resonance; B_{m} is field modulation amplitude; ω_{m} is field modulation frequency; t represents time; and $\vec{G}$ is the spatially linear magnetic field gradient.

For the RF excitation frequency ω_c and gyromagnetic ratio γ, the condition $\omega_c = \gamma B_{\mathrm{ext}}(\vec{r})$ defines a hyperplane in the spectral-spatial domain over which the magnetic resonance occurs. The measured signal is proportional to the integration of $f_u(\vec{r}, B)$ over this hyperplane. The resulting one-dimensional projection, p, measured as a function of field sweep b, can be written as,

$$p(t; b, \vec{G}, f_u) = c_0 \int_{B_0 - \frac{\Delta B}{2}}^{B_0 + \frac{\Delta B}{2}} \int_{\vec{r}} f_u(\vec{r}, B)\, \delta(B - B_{\mathrm{ext}})\, e^{j\beta(t)}\, d\vec{r}\, dB, \tag{A.4}$$

where c_0 is a scalar constant that represents the net multiplicative signal amplification of the EPR system, the quantity ΔB is the spectral window, and $\beta(t)$ is the microwave phase difference at channels C_1 and C_2 of the ADC at time t. Since the microwave phase difference, for the proposed digital receiver setup [17], changes gradually over time, we can assume the $\beta(t)$ to be constant across each projection and only vary from one projection to another. Let $\beta(\vec{G})$ be the constant but unknown value of the microwave phase difference for a projection identified by its gradient $\vec{G}$. The magnetic field range

$B_0 - \Delta B/2$ to $B_0 + \Delta B/2$ is selected to meet or exceed the spectral support of $f_u(\vec{r}, B)$. Using $\tilde{f}_u(\vec{r}, B) \equiv f_u(\vec{r}, B + B_0)$, we can rewrite Eq. (A.4) as,

$$p(t; b, \vec{G}, f_u) = c_0 \int_{-\frac{\Delta B}{2}}^{\frac{\Delta B}{2}} \int_{\vec{r}} e^{j\beta(\vec{G})}\tilde{f}_u(\vec{r}, B)\, \delta\left(B - b - B_{\mathrm{m}}\cos(\omega_{\mathrm{m}} t) - \vec{G} \cdot \vec{r}\right) d\vec{r}\, dB$$

$$= c_0 \int_{-\frac{\Delta B}{2}}^{\frac{\Delta B}{2}} \int_{\vec{r}} e^{j\tilde{\alpha}_u(\vec{G})}\mathcal{E}_u(\vec{r})\widetilde{\mathcal{L}}_u(B)\,\delta\left(B - b - B_{\mathrm{m}}\cos(\omega_{\mathrm{m}} t) - \vec{G} \cdot \vec{r}\right) d\vec{r}\, dB, \tag{A.5}$$

where $\widetilde{\mathcal{L}}_u(B) = \widetilde{\mathcal{L}}_u(B + B_0)$ and $\tilde{\alpha}_u(\vec{G}) = \alpha_u + \beta(\vec{G})$.

To extract the kth field modulation harmonic, $p(t; b, \vec{G}, f)$ is multiplied with $\cos(k\omega_{\mathrm{m}} t)$ and averaged over time for each value of b. Let $p_k(b; \vec{G}, f_u)$ be the complex kth harmonic given by

$$p_k(b; \vec{G}, f_u) = c_0 \int_{\frac{-\pi}{\omega_{\mathrm{m}}}}^{\frac{-\pi}{\omega_{\mathrm{m}}}} \int_{-\frac{\Delta B}{2}}^{\frac{\Delta B}{2}} \int_{\vec{r}} e^{j\tilde{\alpha}_u(\vec{G})}\mathcal{E}_u(\vec{r})\widetilde{\mathcal{L}}_u(B)\delta(B - b - B_{\mathrm{m}}\cos(\omega_{\mathrm{m}} t)$$

$$- \vec{G} \cdot \vec{r})\cos(k\omega_{\mathrm{m}} t)\, dt\, d\vec{r}\, dB$$

$$= c_0 \int_{\frac{-\pi}{\omega_{\mathrm{m}}}}^{\frac{-\pi}{\omega_{\mathrm{m}}}} \int_{-\frac{\Delta B}{2}}^{\frac{\Delta B}{2}} \int_{\vec{r}} e^{j\tilde{\alpha}_u(\vec{G})}\mathcal{E}_u(\vec{r})\widetilde{\mathcal{L}}_u(B + B_{\mathrm{m}}\cos(\omega_{\mathrm{m}} t))\delta$$

$$\times (B - b - \vec{G} \cdot \vec{r})\cos(k\omega_{\mathrm{m}} t)\, dt\, d\vec{r}\, dB$$

$$= c_0 \int_{-\frac{\Delta B}{2}}^{\frac{\Delta B}{2}} \int_{\vec{r}} e^{j\tilde{\alpha}_u(\vec{G})}\mathcal{E}_u(\vec{r}) \int_{\frac{-\pi}{\omega_{\mathrm{m}}}}^{\frac{-\pi}{\omega_{\mathrm{m}}}} \widetilde{\mathcal{L}}_u(B + B_{\mathrm{m}}\cos(\omega_{\mathrm{m}} t))$$

$$\times \cos(k\omega_{\mathrm{m}} t)\, dt\,\delta(B - b - \vec{G} \cdot \vec{r})\, d\vec{r}\, dB$$

$$= c_0 \int_{-\frac{\Delta B}{2}}^{\frac{\Delta B}{2}} \int_{\vec{r}} e^{j\tilde{\alpha}_u(\vec{G})}\mathcal{E}_u(\vec{r})\widetilde{\mathcal{L}}_{u,k}(B)\,\delta(B - b - \vec{G} \cdot \vec{r})\, d\vec{r}\, dB, \tag{A.6}$$

where $\widetilde{\mathcal{L}}_{u,k}(B) = \int_{-\frac{\pi}{\omega_{\mathrm{m}}}}^{\frac{-\pi}{\omega_{\mathrm{m}}}} \widetilde{\mathcal{L}}_u(B + B_{\mathrm{m}}\cos(\omega_{\mathrm{m}} t))\cos(k\omega_{\mathrm{m}} t)\, dt$ is the modulation distorted complex lineshape for the kth harmonic [25].

Let us introduce a new variable, $\theta \in \left(-\frac{\pi}{2}, \frac{\pi}{2}\right)$, called spectral angle and define it as

$$\tan\theta \equiv \frac{\vec{G}}{v\widehat{G}} = \frac{G}{v}, \tag{A.7}$$

where G is the gradient magnitude, $\widehat{G}$ is the unit vector defining gradient orientation, and $v = \Delta B / \Delta L$ is scalar constant with ΔL being the diameter of the spatial FOV. By expressing $\vec{G}$ in terms of θ, we can write Eq. (A.6) as

$$p_k\left(b; \vec{G}, f_u\right) = c_0 \int_{-\frac{\Delta B}{2}}^{\frac{\Delta B}{2}} \int_{\vec{r}} e^{j\tilde{\alpha}_u(\vec{G})}\mathcal{E}_u(\vec{r})\widetilde{\mathcal{L}}_{u,k}(B)\,\delta\left(b - B + v\widehat{G} \cdot \vec{r}\tan\theta\right) d\vec{r}\, dB$$

$$= c_1 \int_{-\frac{\Delta B}{2}}^{\frac{\Delta B}{2}} \int_{\vec{r}} e^{j\tilde{\alpha}_u(\vec{G})}\mathcal{E}_u(\vec{r})\widetilde{\mathcal{L}}_{u,k}(B)\,\delta\left(\frac{b - B}{v\tan\theta} + \widehat{G} \cdot \vec{r}\right) d\vec{r}\, dB, \tag{A.8}$$

where $c_1 = \frac{c_0}{|v\tan\theta|}$ is a revised constant. By $\widetilde{B} \equiv \frac{B\cos\theta}{v}$ and $\rho \equiv \frac{b\cos\theta}{v}$, we can express p in Eq. (A.8) by

$$p_k\left(\rho; \vec{G}, f_u\right) = c_2 \int_{-\frac{\widetilde{\Delta B}}{2}}^{\frac{\widetilde{\Delta B}}{2}} \int_{\vec{r}} e^{j\tilde{\alpha}_u(\vec{G})}\mathcal{E}_u(\vec{r})\widetilde{\mathcal{L}}_{u,k}\left(\frac{v\widetilde{B}}{\cos\theta}\right)\delta\left(\frac{\rho - \widetilde{B}}{\sin\theta} + \widehat{G} \cdot \vec{r}\right) d\vec{r}\, d\widetilde{B}$$

$$= c_2 \int_{-\frac{\widetilde{\Delta B}}{2}}^{\frac{\widetilde{\Delta B}}{2}} e^{j\tilde{\alpha}_u(\vec{G})}\widetilde{\mathcal{L}}_{u,k}\left(\frac{v\widetilde{B}}{\cos\theta}\right)\int_{\vec{r}} \mathcal{E}_u(\vec{r})\,\delta\left(\frac{\rho - \widetilde{B}}{\sin\theta} + \widehat{G} \cdot \vec{r}\right) d\vec{r}\, d\widetilde{B}, \tag{A.9}$$

with $\Delta\widetilde{B} = \frac{\Delta B\cos\theta}{v}$, and $c_2 = \frac{c_1|v|}{|\cos\theta|}$.

The inner integral of Eq. (A.9) represents the spatial profile of $\mathcal{E}_u(\vec{r})$, computed by the Radon transform. The plane of integration $\frac{\rho - \widetilde{B}}{\sin\theta} + \widehat{G} \cdot \vec{r} = 0$ resides in $\vec{r}$ with its orientation determined by $\widehat{G}$. Practically, the integral is approximated by a weighted summation under a suitable basis function representation of $\mathcal{E}_u(\vec{r})$, which is otherwise continuous. In this work, we have used piece-wise

constant square (or cubic) pixels (or voxels) to express $\mathcal{E}_u(\vec{r})$. By denoting this spatial projection as $s\left(\frac{\rho-\widetilde{B}}{\sin\theta};\widehat{G},\mathcal{E}_u\right)$, we get

$$p_k\left(\rho;\overrightarrow{G},f_u\right) = c_2 \int_{-\frac{\Delta B}{2}}^{\frac{\Delta B}{2}} e^{j\tilde{\alpha}_u(\overrightarrow{G})} \widetilde{\mathcal{L}}_{u,k}\left(\frac{\nu\widetilde{B}}{\cos\theta}\right) s\left(\frac{\rho-\widetilde{B}}{\sin\theta};\widehat{G},\mathcal{E}_u\right) d\widetilde{B}$$

$$= c_2 e^{j\tilde{\alpha}_u(\overrightarrow{G})} \widetilde{\mathcal{L}}_{u,k}\left(\frac{\nu\rho}{\cos\theta}\right) * s\left(\frac{\rho}{\sin\theta};\widehat{G},\mathcal{E}_u\right), \qquad (A.10)$$

where $*$ represents convolution with respect to ρ. If the sweep range of b is set from $\frac{-\Delta B}{2\cos\theta}$ to $\frac{\Delta B}{2\cos\theta}$, which is generally the case for most EPR systems, the range of ρ becomes independent of spectral angle θ and is equal to ΔL. If $n = 0, 1, \ldots, N-1$ represents discretization of ρ, for a high enough sampling rate, we can rewrite Eq. (A.10) as

$$p_k\left(n;\overrightarrow{G},f_u\right) \approx \tilde{p}_k\left(n;\overrightarrow{G},f_u\right) \equiv c_3 e^{j\tilde{\alpha}_u(\overrightarrow{G})} \widetilde{\mathcal{L}}_{u,k}\left(\frac{\Delta B_n}{\cos\theta}\right) * s\left(\frac{\Delta L_n}{\sin\theta};\widehat{G},\mathcal{E}_u\right),$$
$$(A.11)$$

where $\Delta B_n = \frac{-\Delta B}{2} + n\frac{\Delta B}{N-1}$, $\Delta L_n = \frac{-\Delta L}{2} + n\frac{\Delta L}{N-1}$, and c_3 is a revised constant which depends on c_2 and the sampling rate for ρ. The output at channel I, $\tilde{p}_{I,k}(n;\overrightarrow{G},f_u)$, and channel Q, $\tilde{p}_{Q,k}(n;\overrightarrow{G},f_u)$, are given by

$$\tilde{p}_{I,k}\left(n;\overrightarrow{G},f_u\right) = \mathrm{Re}\left(\tilde{p}_k\left(n;\overrightarrow{G},f_u\right)\right) = c_3\left(\widetilde{\mathcal{L}}_{u,k}^a\left(\frac{\Delta B_n}{\cos\theta}\right)\cos\left(\tilde{\alpha}_u(\overrightarrow{G})\right)\right.$$
$$\left. -\widetilde{\mathcal{L}}_{u,k}^d\left(\frac{\Delta B_n}{\cos\theta}\right)\sin\left(\tilde{\alpha}_u(\overrightarrow{G})\right)\right) * s\left(\frac{\Delta L_n}{\sin\theta};\widehat{G},\mathcal{E}_u\right)$$

$$\tilde{p}_{Q,k}\left(n;\overrightarrow{G},f_u\right) = \mathrm{Im}\left(\tilde{p}_k\left(n;\overrightarrow{G},f_u\right)\right), = c_3\left(\widetilde{\mathcal{L}}_{u,k}^d\left(\frac{\Delta B_n}{\cos\theta}\right)\sin\left(\tilde{\alpha}_u(\overrightarrow{G})\right)\right.$$
$$\left. +\widetilde{\mathcal{L}}_{u,k}^d\left(\frac{\Delta B_n}{\cos\theta}\right)\cos\left(\tilde{\alpha}_u(\overrightarrow{G})\right)\right) * s\left(\frac{\Delta L_n}{\sin\theta};\widehat{G},\mathcal{E}_u\right), \quad (A.12)$$

where $\widetilde{\mathcal{L}}_{u,k}^a = \mathrm{Re}(\widetilde{\mathcal{L}}_{u,k})$ and $\widetilde{\mathcal{L}}_{u,k}^d = \mathrm{Im}(\widetilde{\mathcal{L}}_{u,k})$. When $\tilde{\alpha}_u(\overrightarrow{G}) = 0$, channel I produces purely absorption while channel Q produces purely dispersion components. The horizontal compression of s by a factor of $1/\sin\theta$ requires interpolation, which can potentially introduce errors. However, by increasing the radial sampling rate of s, the interpolation error can be reduced to an arbitrarily low value.

A multisite spectral-spatial object f can be considered as a summation of all subobjects. Therefore, the measured harmonic data at I and Q channels can be written as

$$y_{I,k}\left(n;\overrightarrow{G}\right) \equiv \sum_{u=1}^{U} \tilde{p}_{I,k}\left(n;\overrightarrow{G},f_u\right) + \eta_I(n),$$
$$y_{Q,k}\left(n;\overrightarrow{G}\right) \equiv \sum_{u=1}^{U} \tilde{p}_{Q,k}\left(n;\overrightarrow{G},f_u\right) + \eta_Q(n), \qquad (A.13)$$

where η_I and η_Q are additive white Gaussian noise.

Appendix B. Incoherent reconstruction for stage 1

In this section, we describe an incoherent reconstruction scheme used in stage 1 to approximate EPR probe spin density distribution. Previously, we linearized the forward model by assuming we known all parameters except for the spin density and solved the spin density using ℓ_1 regularized least-squares [20]. Unfortunately, the value for the microwave may vary across space and time, and reconstruction based on a single arbitrarily assigned value of the microwave may result is a poor quality reconstruction for stage 1.

For the proposed incoherent reconstruction of stage 1, we assume the following: (i) image is decomposed into M pixels (voxels) and each image pixel (voxel) is represented by a Dirac delta function located at the center and (ii) all parameters except for the microwave phase and spin density are known and are spatially and temporally invariant.

Let's reconsider the entire multisite object f and assign suitable values to all unknown parameters except for the spin density, $\mathcal{E}(\vec{r})$, and microwave phase. We assume the microwave phase is unknown and varies not only from projection to projection but also with space. Under these assumptions, Eq. (A.8) becomes

$$p_k\left(b;\overrightarrow{G},f\right) = c_0 \int_{-\frac{\Delta B}{2}}^{\frac{\Delta B}{2}} \int_{\vec{r}} e^{j\tilde{\alpha}(\vec{r},\overrightarrow{G})}\mathcal{E}(\vec{r})\widetilde{\mathcal{L}}_k(B)\delta\left(b-B+\nu\widehat{G}\cdot\vec{r}\tan\theta\right) d\vec{r}dB$$

$$= c_0 \int_{\vec{r}} e^{j\tilde{\alpha}(\vec{r},\overrightarrow{G})}\mathcal{E}(\vec{r})\widetilde{\mathcal{L}}_k\left(b+\nu\widehat{G}\cdot\vec{r}\tan\theta\right) d\vec{r}. \qquad (B.1)$$

where $\tilde{\alpha}(\vec{r},\overrightarrow{G}) = \alpha(\vec{r})\beta(\overrightarrow{G})$.

Under a Dirac delta representation of the pixels (or voxels) and discretization of b into N steps, Eq. (B.1) simplifies to a summation, generating

$$p_k\left(n;\overrightarrow{G},f\right) \approx \acute{p}_k\left(n;\overrightarrow{G},f\right)$$
$$\equiv c_0 \sum_{m=1}^{M} e^{j\tilde{\alpha}(\vec{r}_m,\overrightarrow{G})}\mathcal{E}(\vec{r}_m)\widetilde{\mathcal{L}}_k\left(\frac{\Delta B_n}{\cos\theta}+\nu\widehat{G}\cdot\vec{r}_m\tan\theta\right), \qquad (B.2)$$

where $m = 0, 1, \ldots, M-1$ represents pixel index, $n = 0, 1, \ldots, N-1$ is the magnetic field sweep index. In matrix form Eq. (B.2) can be written as

$$\begin{bmatrix} \acute{p}_{I,k}\left(\overrightarrow{G},f\right) \\ \acute{p}_{Q,k}\left(\overrightarrow{G},f\right) \end{bmatrix} = \begin{bmatrix} A_{k,\overrightarrow{G}} & -D_{k,\overrightarrow{G}} \\ D_{k,\overrightarrow{G}} & A_{k,\overrightarrow{G}} \end{bmatrix}$$
$$\times \begin{bmatrix} E^{\mathrm{Re}}\cos\left(\beta(\overrightarrow{G})\right) - E^{\mathrm{Im}}\sin\left(\beta(\overrightarrow{G})\right) \\ E^{\mathrm{Re}}\cos\left(\beta(\overrightarrow{G})\right) + E^{\mathrm{Im}}\sin\left(\beta(\overrightarrow{G})\right) \end{bmatrix}, \qquad (B.3)$$

where $\acute{p}_{I,k}(\overrightarrow{G},f) = [\mathrm{Re}(\acute{p}_k(n;\overrightarrow{G},f))]_n$ and $\acute{p}_{Q,k}(\overrightarrow{G},f) = [\mathrm{Im}(\acute{p}_k(n;\overrightarrow{G},f))]_n$ are $N \times 1$ vectors; $E^{\mathrm{Re}} = [\mathrm{Re}(\mathcal{E}(\vec{r}_m)e^{j\alpha(\vec{r}_m)})]_m$ and $E^{\mathrm{Im}} = [\mathrm{Im}(\mathcal{E}(\vec{r}_m)e^{j\alpha(\vec{r}_m)})]_m$ are $M \times 1$ vectors; and $A_{k,\overrightarrow{G}}$ and $D_{k,\overrightarrow{G}}$ are $N \times M$ matrices defined by

$$A_{k,\overrightarrow{G}} = \left[\mathrm{Re}\left(\widetilde{\mathcal{L}}_k\left(\frac{\Delta B_n}{\cos\theta}+\nu\widehat{G}\cdot\vec{r}_m\tan\theta\right)\right)\right]_{n,m},$$
$$D_{k,\overrightarrow{G}} = \left[\mathrm{Im}\left(\widetilde{\mathcal{L}}_k\left(\frac{\Delta B_n}{\cos\theta}+\nu\widehat{G}\cdot\vec{r}_m\tan\theta\right)\right)\right]_{n,m}.$$

If there is no variation in α from projection to projection, equations from different projections can be concatenated to form a $2NPk \times 2M$ set of equations, with P being the number of projections, and can be solved using ℓ_1 regularized least-squares. However, directly solving (B.3) when β varies from projection to projection often provides poor quality images.

By $A_{k,\overrightarrow{G}}^- \equiv \left[A_{k,\overrightarrow{G}} - D_{k,\overrightarrow{G}}\right]$ and $A_{k,\overrightarrow{G}}^+ \equiv \left[D_{k,\overrightarrow{G}} A_{k,\overrightarrow{G}}\right]$, we can show that

$$\left(\acute{p}_{I,k}\left(\overrightarrow{G},f\right)\right)^{\succ 2} + \left(\acute{p}_{Q,k}\left(\overrightarrow{G},f\right)\right)^{\succ 2} = \left(A_{k,\overrightarrow{G}}^- \begin{bmatrix} E^{\mathrm{Re}} \\ E^{\mathrm{Im}} \end{bmatrix}\right)^{\succ 2} + \left(A_{k,\overrightarrow{G}}^+ \begin{bmatrix} E^{\mathrm{Re}} \\ E^{\mathrm{Im}} \end{bmatrix}\right)^{\succ 2},$$
$$(B.4)$$

where the notation $\succ$ indicates the operation is performed on an element-by-element basis. By concatenating all harmonics and all projections, we can write $NPk \times 2M$ nonlinear equations

$$\left(\acute{p}_I(f)\right)^{\succ 2} + \left(\acute{p}_Q(f)\right)^{\succ 2} = \left(A^- \begin{bmatrix} E^{\mathrm{Re}} \\ E^{\mathrm{Im}} \end{bmatrix}\right)^{\succ 2} + \left(A^+ \begin{bmatrix} E^{\mathrm{Re}} \\ E^{\mathrm{Im}} \end{bmatrix}\right)^{\succ 2}. \qquad (B.5)$$

The absence of k and $\overrightarrow{G}$ in Eq. (B.5) indicates that all the harmonics and projections has been concatenated to generate $\acute{p}_I$, $\acute{p}_Q$, A^-, and A^+. Let $\mathcal{C}$ represents the right side of (B.5) and $\mathcal{Y} \equiv (y_I(f))^{\succ 2} +$

$(y_Q(f))^{-2}$, with $y_I(f)$ and $y_Q(f)$ being all the measurements at channel I and channel Q in vector forms; then we can solve for I^{Re} and E^{Im} using nonlinear least-squares

$$\begin{bmatrix} \widehat{E}^{Re} \\ \widehat{E}^{Im} \end{bmatrix} = \operatorname*{argmin}_{E^{Re}, E^{Im}} \left\| \mathcal{C}^{-\frac{1}{2}} - \mathcal{Y}^{-\frac{1}{2}} \right\|_2^2 + \lambda \left\| \begin{bmatrix} E^{Re} \\ E^{Im} \end{bmatrix} \right\|_1^1, \tag{B.6}$$

where a positive constant λ controls the regularization. The estimate of the spin density distribution, $\widehat{E}$, can be obtained by

$$\widehat{E} = \left(\left(E^{Re} \right)^{-2} + \left(E^{Im} \right)^{-2} \right)^{-\frac{1}{2}}. \tag{B.7}$$

References

[1] A. Kulkarni, P. Kuppusamy, N. Parinandi, Oxygen, the lead actor in the pathophysiologic drama: enactment of the trinity of normoxia, hypoxia, and hyperoxia in disease and therapy, Antioxid. Redox Signaling 9 (2007) 1717–1730.
[2] K. Selvendiran, A. Bratasz, M. Kuppusamy, M. Tazi, B. Rivera, P. Kuppusamy, Hypoxia induces chemoresistance in ovarian cancer cells by activation of signal transducer and activator of transcription 3, Int. J. Cancer 125 (2009) 2198–2204.
[3] H. Hopf, J. Gibson, A. Angeles, J. Constant, J. Feng, M. Rollins, M.Z. Hussain, T. Hunt, Hyperoxia and angiogenesis, Wound Repair Regen. 13 (2005) 558–564.
[4] R. Ahmad, P. Kuppusamy, Theory, instrumentation, and applications of electron paramagnetic resonance oximetry, Chem. Rev. (2010) 3212–3236.
[5] B. Gallez, K. MSder, H. Swartz, Noninvasive measurement of the pH inside the gut by using pH-sensitive nitroxides. An in vivo EPR study, Magn. Reson. Med. 36 (1996) 694–697.
[6] B. Gallez, G. Bacic, F. Goda, J. Jiang, J. O'Hara, J. Dunn, H. Swartz, Use of nitroxides for assessing perfusion, oxygenation, and viability of tissues: in vivo EPR and MRI studies, Magn. Reson. Med. 35 (1996) 97–106.
[7] N. Khan, D. Das, Application of in vivo EPR for tissue pO2 and redox measurements, Methods Mol. Biol. 559 (2009) 131–139.
[8] A. Dikalova, M. Kadiiska, R. Mason, An in vivo ESR spin-trapping study: free radical generation in rats from formate intoxication role of the Fenton reaction, Proc. Natl. Acad. Sci. U. S. A. 98 (2001) 1354913553.
[9] M. Eastman, R. Kooser, M. Das, J. Freed, Studies of heisenberg spin exchange in ESR spectra. I. Linewidth and saturation effects, J. Chem. Phys. 51 (1969) 2690–2709.
[10] Y. Deng, R. Pandian, R. Ahmad, P. Kuppusamy, J. Zweier, Application of magnetic field over-modulation for improved EPR linewidth measurements using probes with Lorentzian lineshape, J. Magn. Reson. 181 (2006) 254–261.
[11] H. Sato-Akaba, Y. Kuwahara, H. Fujii, H. Hirata, Half-life mapping of nitroxyl radicals with three-dimensional electron paramagnetic resonance imaging at an interval of 3.6 s, Anal. Chem. 81 (2009) 7501–7506.
[12] J. Joshi, J. Ballard, G. Rinard, R. Quine, S. Eaton, G. Eaton, Rapid-scan EPR with triangular scans and Fourier deconvolution to recover the slow-scan spectrum, J. Magn. Reson. 175 (2005) 44–51.
[13] B. Epel, S. Sundramoorthy, C. Mailer, H. Halpern, A versatile high speed 250 MHz pulse imager for biomedical applications, Concepts Magn. Reson. Part B: Magn. Reson. Eng. 33B (2008) 163–176.
[14] S. Som, L. Potter, R. Ahmad, P. Kuppusamy, A parametric approach to spectral-spatial EPR imaging, J. Magn. Reson. 186 (2007) 1–10.
[15] R. Ahmad, D. Vikram, B. Clymer, L. Potter, Y. Deng, P. Srinivasan, J. Zweier, P. Kuppusamy, Uniform distribution of projection data for improved reconstruction quality of 4D EPR imaging, J. Magn. Reson. 187 (2007) 277–287.
[16] J. Hyde, H. Mchaourab, T. Camenisch, J. Ratke, R. Cox, W. Froncisz, EPR detection by time-locked sub-sampling, Rev. Sci. Instrum. 69 (1998) 2622–2628.
[17] R. Ahmad, S. Som, E. Kesselring, P. Kuppusamy, J. Zweier, L. Potter, Digital detection and processing of multiple quadrature harmonics for EPR spectroscopy, J. Magn. Reson. 207 (2010) 322–331.
[18] M. Tseitlin, V. Iyudin, O. Tseitlin, Advantages of digital phase-sensitive detection for upgrading an obsolete CW EPR spectrometer, Appl. Magn. Reson. 35 (2009) 569–580.
[19] O. Grinberg, A. Smirnov, H. Swartz, High spatial resolution multi-site EPR oximetry: the use of a convolution-based fitting method, J. Magn. Reson. 152 (2001) 247–258.
[20] S. Som, L. Potter, R. Ahmad, D. Vikram, P. Kuppusamy, EPR oximetry in three spatial dimensions using sparse spin distribution, J. Magn. Reson. 193 (2008) 210–217.
[21] B. Leugn, The oversampling technique for analog to digital conversion: a tutorial overview, Analog Integr. Circ. Signal Process. 1 (1991) 65–74.
[22] M. Alecci, S. McCallum, D. Lurie, Design and optimization of an automatic frequency control system for a radiofrequency electron paramagnetic resonance spectrometer, J. Magn. Reson. 117 (1995) 272–277.
[23] A. Smirnov, S. Norby, R. Clarkson, H. Swartz, Simultaneous multi-site EPR spectroscopy in vivo, Magn. Reson. Med. (1993) 213–220.
[24] B. Williams, H. Hou, O. Grinberg, E. Demidenko, H. Swartz, High spatial resolution multisite EPR oximetry of transient focal cerebral ischemia in the rat, Antioxid. Redox Signal (2007) 1691–1698.
[25] B. Robinson, C. Mailer, A. Reese, Linewidth analysis of spin labels in liquids: I. Theory and data analysis, J. Magn. Reson. 138 (1999) 199–209.
[26] R. Ahmad, G. Caia, L. Potter, S. Petryakov, P. Kuppusamy, J. Zweier, In vivo multisite oximetry using EPR-NMR coimaging, J. Magn. Reson. 207 (2010) 69–77.
[27] A. Smirnov, T. Smirnova, Convolution-based Algorithms: From Analysis to Rotational Dynamics to EPR Oximetry and Protein Distance Measurements, Kluwer Academic, 2004. pp. 277–348 (Chapter 6).
[28] R. Pandian, N. Parinandi, G. Ilangovan, J. Zweier, P. Kuppusamy, Novel particulate spin probe for targeted determination of oxygen in cells and tissues, Free Radical Biol. Med. 35 (2003) 1138–1148.
[29] J. Hyde, T. Camenisch, J. Ratke, R. Strangeway, W. Froncisz, Biomedical EPR, Part B: Methodology, Instrumentation, and Dynamics, Springer, New York, 2004.
[30] R. Nielsen, E. Hustedt, A. Beth, B. Robinson, Formulation of Zeeman modulation as a signal filter, J. Magn. Reson. 170 (2004) 345–371.
[31] M. Tseitlin, S. Eaton, G. Eaton, Reconstruction of the first-derivative EPR spectrum from multiple harmonics of the field-modulated continuous wave signal, J. Magn. Reson. 209 (2011) 277–281.